A Liquid-like Quasi-solid Polymer Electrolyte for High-performance Sodium Metal Batteries

Journal:	*Journal of Materials Chemistry A*
Manuscript ID	TA-ART-03-2025-002012.R1
Article Type:	Paper
Date Submitted by the Author:	06-May-2025
Complete List of Authors:	Vineeth, S.; Indian Institute of Technology Delhi, Soni, Chhail Bihari; Indian Institute of Technology Delhi, Energy Studies ., Sungjemmenla; Indian Institute of Technology Delhi, Energy Science and Engineering; Indian Institute of Technology Delhi, Energy Science and Engineering Chandra, Mahesh ; Indian Institute of Technology Delhi, Physics; Indian Institute of technology Indore Sanjaykumar, C.; Indian Institute of Technology Delhi, Bhandari, Arihant; Indian Institute of Technology Delhi Yamauchi, Yusuke; University of Queensland, Chemical Engineering; Nagoya University, Han, Minsu; Yonsei University, Chemical and Biomolecular Engineering; The University of Queensland Australian Institute for Bioengineering and Nanotechnology, Kumar, Vipin; Indian Institute of Technology Delhi, Department of energy science and engineering

A Liquid-like Quasi-solid Polymer Electrolyte for High-performance Sodium Metal Batteries

Vineeth Sasikumar Kala,[1,2,3] Chhail Bihari Soni,[1] Sungjemmenla,[1] Mahesh Chandra,[1] Sanjaykumar C.,[1] Arihant Bhandari,[1] Yusuke Yamauchi,[3,4,5] Minsu Han,[3,4]* and Vipin Kumar[1,2]*

[1]Department of Energy Science and Engineering, Indian Institute of Technology Delhi, Hauz Khas, New Delhi, India 110016

[2]University of Queensland- IIT Delhi Academy of Research (UQIDAR), Indian Institute of Technology Delhi, Hauz Khas, New Delhi, India 110016

[3]Australian Institute for Bioengineering and Nanotechnology (AIBN), The University of Queensland, Brisbane, QLD 4072, Australia

[4]Department of Materials Process Engineering, Graduate School of Engineering, Nagoya University, Nagoya 464-8603, Japan

[5]Department of Chemical and Biomolecular Engineering, Yonsei University, 50 Yonsei-ro, Seodaemun-gu, Seoul 03722, Republic of Korea

Corresponding author E-mail - vkumar@dese.iitd.ac.in, minsu.han@uq.edu.au

Abstract

Conventional liquid electrolytes cannot adequately ensure the safety of sodium metal batteries (SMBs), making quasi-solid polymer electrolytes (QSPEs) attractive alternatives. Herein, we introduce a QSPE that exhibits liquid-level ionic conductivity with the mechanical robustness of a solid polymer electrolyte. Optimizing the ratio of poly(vinylidene fluoride-co-hexafluoropropylene) and poly(ethylene glycol)-block-poly(propylene glycol)-block-poly(ethylene glycol) yields a “liquid-like” electrolyte exhibiting a room-temperature ionic conductivity of 1.01 mS cm^{-1}, a Na$^+$ transference number of 0.78, and a glass-transition temperature of 22.5°C. Raman spectroscopy shows that the electron-donating -C-O-C- units promote the formation of aggregated ion pairs, enabling an inorganic-rich interphase. Density functional theory calculations predict that fluoride-containing reduction products form more readily than non-fluorinated counterparts, leading to the formation of a stable solid electrolyte interphase and the suppression of dendritic growth. Molecular dynamics (MD) simulations give insights into the solvation environment and coordination of Na^+ ions with electron-withdrawing groups. Simulations also predict high ionic conductivity and transference numbers, confirming the high ion transport in the QSPE seen experimentally. Consistent with these insights, a Na//Na symmetric cell cycles stably for 200 h at high current density with superior charge transfer proficiency, while a Na//Prussian blue full cell delivers an initial capacity of 159 mAh g^{-1} at 0.5 C and retains outstanding performance over 500 cycles. These findings underscore the importance of judicious polymer blending in advancing high-performance SMBs.

Keywords: Polymer blends; Quasi-solid state polymer electrolytes; Activation energy; Solvation; Sodium metal battery

1. Introduction

Owing to its high theoretical specific capacity and low redox potential (-2.71 V vs standard hydrogen electrode), sodium metal is a compelling anode for the post-lithium-ion era [1] Sodium-metal batteries (SMBs) can surpass lithium-ion batteries in energy density and cost per kWh [2]. Yet, SMBs that employ conventional liquid electrolytes (LEs) face major safety issues electrolyte leakage, flammability, and dendritic Na growth that can short-circuit the cell [3]. Parasitic reactions between the Na anode and the LE also corrode the metal during cycling, forming an unstable solid electrolyte interphase (SEI) [4]. Because the physicochemical properties of SEI largely dictate battery performance [5], many strategies have been explored to stabilize it, including artificial SEI layers formed by additives, high-concentration electrolytes, and solvation-structure regulation to create inorganic-rich SEI [6–11]. Nonetheless, these techniques do not fully eliminate the intrinsic drawbacks of LE systems.

Recent work has focused on solid-state and, in particular, quasi-solid polymer electrolytes (QSPEs), which combine superior thermo-mechanical strength with effective suppression of dendrite growth [12,13]. Unlike glass fiber separators that merely absorb LE, QSPEs feature a polymeric backbone that can be engineered into a porous network capable of retaining LE [14]. This solid-liquid hybrid preserves the high ionic conductivity, elevated transference number, and low interfacial resistance typical of liquid systems while possessing the enhanced thermal, chemical, and mechanical robustness of solid separators [15,16] The interconnected porosity of QSPEs also promotes electrolyte uptake and retention, facilitating rapid ion transport and further mitigating dendrite formation [17,18]. Crucially, the performance of QSPEs can be tuned by tailoring the host matrix or incorporating functional additives; excessive crystallinity in the polymer, however, restricts segmental motion and thereby limits ionic transportation [19]. Strategies to lower the polymer crystallinity include copolymerization, the incorporation of nanofillers, disruption of the chain orientation, and blending with a second polymer [20]. When two miscible polymers are combined in an optimized ratio, cooperative interactions can deliver properties superior to either constituent alone [21]. Such interactions enhance amorphous character and chain mobility, thereby boosting ionic conductivity [22]. As ionic mobility directly governs electrochemical kinetics, enhancing ion transport accelerates the overall battery performance. Accordingly, judicious polymer blending that raises ionic conductivity and transference number while tailoring solvation chemistry to promote a robust SEI can transform conventional QSPEs into a “liquid-like” QSPE for next-generation SMBs.

Polyvinylidene fluoride (PVDF) and its copolymer poly (vinylidene fluoride-co-hexafluoropropylene) (PVDF-HFP) are among the most widely utilized polymer hosts for Na^+ conduction [23]. Their strong affinity for LEs, robust thermo-mechanical properties, and wide electrochemical stability window (ESW) make them attractive for SMBs. The abundance of electron-withdrawing fluorine atoms endows these polymers with a high dielectric constant (8.4), which promotes salt dissociation [24]. However, both PVDF and PVDF-HFP are semi-crystalline; amorphous domains are confined between crystalline lamellae that severely restrict ion transport [24]. Blending them with other materials has emerged as an effective strategy to expand the amorphous phase and enhance ionic conductivity [21,24]. For example, Wunder *et al.* blended PVDF-HFP with pentaerythritol tetrakis (3-mercaptopropionate) and pentaerythritol tetra acrylate for SMB application [25]. The system achieved an ionic conductivity of 1.4×10^{-5} mS cm^{-1} at 20°C and an ESW of 4.5 V (*vs.* Na/Na^+).

However, comprehensive studies of novel PVDF-HFP blends and their effects on crystallinity, ionic mobility, and interfacial modification of SEIs are still scarce. Herein, we introduce a blend of PVDF-HFP with the triblock copolymer, poly(ethylene glycol)-block-poly(propylene glycol)-block-poly(ethylene glycol) (PEG-PPG-PEG). This copolymer features hydrophilic PEG end blocks flanking a hydrophobic PPG mid-block. The electron-donating -C-O-C- groups enhance Na-salt solubility and adjust the solvation environment through inductive and resonance effects. PEG-PPG-PEG also acts as a plasticizer, lowering the crystallinity of PVDF-HFP and thereby promoting ion transport. Free-standing polymer hosts have been prepared by blending PVDF-HFP with PEG-PPG-PEG at various weight ratios, and their ionic mobility is investigated after activation with a LE. Crystallinity decreases steadily as the triblock copolymer content increases, while electrolyte uptake and porosity rise sharply. The optimized blend QSPE (70 wt.% PVDF-HFP/30 wt.% PEG-PPG-PEG) exhibits an ionic conductivity of 1.01 mS cm^{-1} at 25 °C, which is 405% higher than that of the pristine PVDF-HFP. Raman and Fourier-transform infrared (FTIR) spectroscopy confirm liquid-like behavior, showing a larger fraction of aggregated ion pairs (AGGs). Thermo-mechanical tests reveal enhanced robustness, corroborated by uniform sodium deposition and stable, reversible stripping/plating in a Na//Na symmetric cell. Density functional theory (DFT) calculations and molecular dynamics (MD) simulations support these observations, clarifying the favorable solvation environment, high ionic conductivity, and transference number of the electrolyte. A fluoride-rich, anion-derived SEI boost cycling stability. Consequently, a Na//Prussian blue full cell delivers a discharge capacity of 120 mAh g^{-1} for 600 cycles at 0.5 C, retains good rate capability, and maintains an average Coulombic efficiency of 98 %.

2. Results and discussions

Detailed experimental procedures, instrumentation, test parameters, and all relevant equations are provided in the Supplementary information.

2.1 Structural and Chemical Analysis of the QSPEs

Figure 1a depicts how increasing the PEG-PPG-PEG content alters the crystallinity of the parent PVDF-HFP matrix, as revealed by X-ray diffraction (XRD). Pristine PVDF-HFP (denoted as Pristine_100) exhibits characteristic α-phase diffraction peaks at 17.6°, 19.8°, 26.3°, and 39.0°, corresponding to the (100), (020), (110), and (021) planes, respectively [26]. As the PEG-PPG-PEG fraction rises, these peaks broaden and decrease in intensity, indicating a growing amorphous fraction. PEG-PPG-PEG disrupts the α-phase lamellar ordering of PVDF-HFP, promoting chain mobility and enlarging the amorphous fraction. The degree of crystallinity (X_{XRD}, %) was quantified using the method described by Vo et al [26].

$$X_{XRD} = \frac{A}{A_o} \times 100$$

where A is the summed area of all crystalline peaks, and A_o is the total integrated area of all peaks in the XRD pattern. The degree of crystallinity in pristine PVDF-HFP is 33.8%, whereas incorporating 10, 20, 30, and 40 wt.% PEG-PPG-PEG reduces it to 29.1, 21.2, 13.2, and 11.4%, respectively (**Figure S1**). This progressive loss of crystallinity upon blending likely relaxes chain packing and, in turn, promotes ionic conduction.

FTIR of pristine_100 shows characteristic stretching vibrations of the fluorinated backbone at 1405, 1173, and 876 cm^{-1} (**Figure 1b,c**). The 1173 cm^{-1} band arises from C-F stretching vibrations [27]. Notably, the intensity of the 1100 cm^{-1} band attributed to the -C-O-C- bond increases with rising PEG-PPG-PEG content [28], confirming the successful incorporation of the triblock copolymer into the PVDF-HFP matrix. Moreover, the 1068 cm^{-1} band, typical of crystalline PVDF-HFP [27], appears broader and weaker in intensity in the blend system, indicating the amorphous nature of the blend. These FTIR findings corroborate the XRD evidence of enhanced amorphization.

QSPEs were prepared by activating the polymer matrices with a LE composed of 1 M $NaClO_4$ in ethylene carbonate (EC)/dimethyl carbonate (DMC)/fluoroethylene carbonate (FEC), and their physicochemical properties were subsequently evaluated. Among the polymer matrices evaluated, the PVDF-HFP/PEG-PPG-PEG blend containing 30 wt.% triblock copolymers (blend_70-30) shows the greatest electrolyte uptake, absorbing 240% of its own mass after 10 min of immersion (**Figure 1d,e**). Relative to pristine_100, which has 38% of porosity, the blend_70-30 reaches 72% of porosity an increase of nearly 90% (**Figure 1f**). The trends in porosity and electrolyte uptake are consistent for all samples and are likewise reflected in their ionic conductivities (**Figure 1g**). Blend_70-30 QSPE records a room-temperature ionic conductivity of 1.01 mS cm^{-1}, 405% higher than that of pristine_100 QSPE (0.20 mS cm^{-1}). This enhanced uptake is attributed to the blend’s larger amorphous fraction. Because cross-sectional thickness also influences physical and electrochemical properties, we optimized the membrane thickness. Ionic-conductivity and electrolyte-uptake analyses show that a 150 μm membrane performs best, and this thickness was adopted for subsequent experiments (**Figure S2**).

Surface morphology was examined by field-emission scanning electron microscopy (FESEM) for both the pristine PVDF-HFP host and blend_70-30 (**Figure 1h,i**). Unlike pristine PVDF-HFP, which presents a rough surface with few pores, blend_70-30 displays an interconnected porous network containing macropores 0.5-2.0 μm in diameter, accounting for its higher porosity. FESEM images at various magnifications confirm that this porous structure is uniform throughout the blend_70-30 matrix, whereas PVDF-HFP membranes exhibit the rough morphology typical of PVDF-HFP (**Figure S3**) [21]. The macropores in blend_70-30 facilitate electrolyte diffusion through the matrix, enlarge the membrane’s active area, and thus increase electrolyte uptake. Elemental mapping indicates that PVDF-HFP and PEG-PPG-PEG are uniformly blended without noticeable agglomeration (**Figures S4** and **S5**). Therefore, the blend_70-30 membrane offers an architecture well-suited for QSPE development.

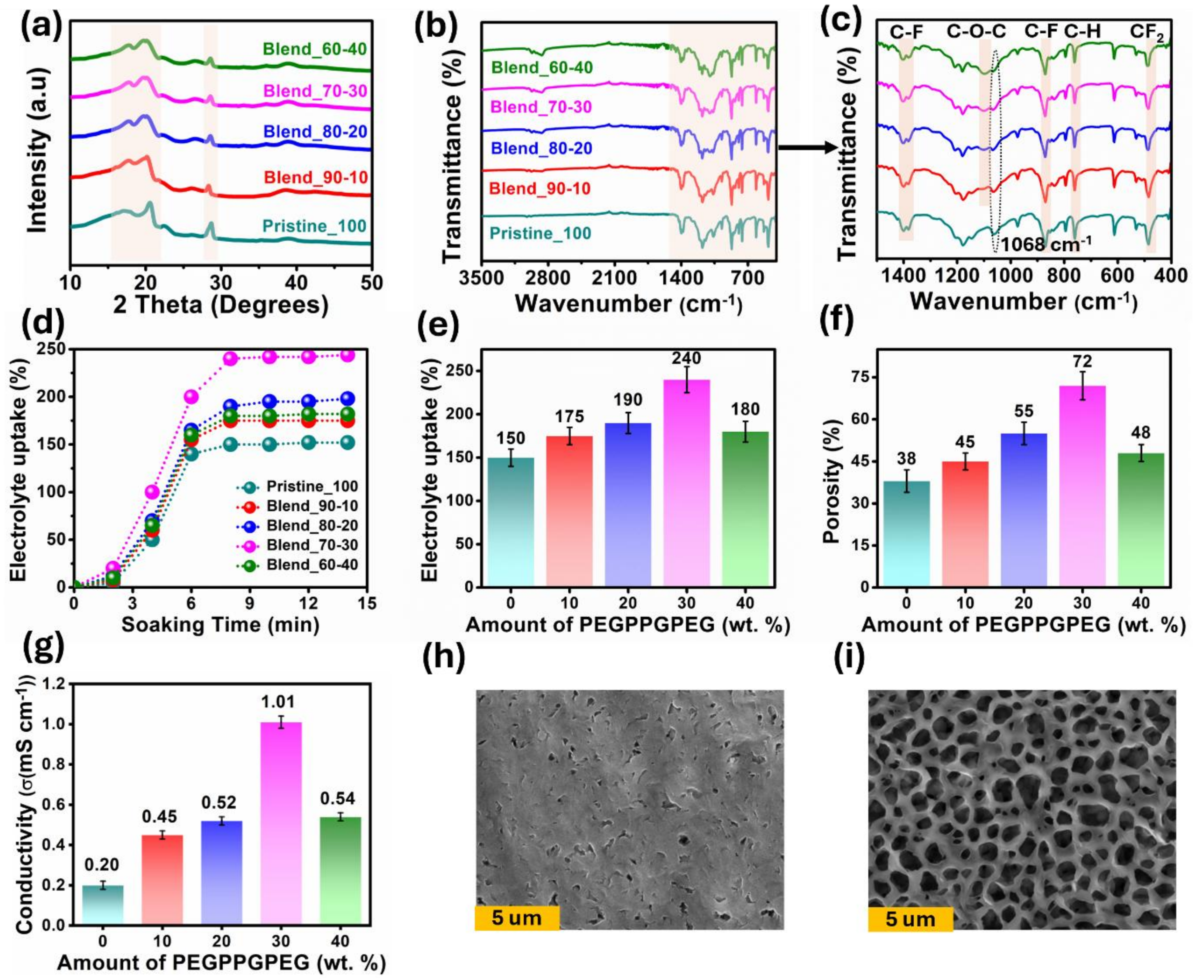

Figure 1. (a) XRD patterns, (b,c) FTIR spectra, (d) time-dependent electrolyte uptake, (e) equilibrium electrolyte uptake, and (f) porosity of the PVDF-HFP and blend membranes. (g) Room-temperature ionic conductivity of the corresponding QSPEs. (h,i) FESEM images of (h) pristine_100 and (i) blend_70-30 membranes.

2.2 Temperature-dependent ionic conduction and thermo-mechanical properties

Figure 2a presents the temperature dependence of ionic conductivity for LE-activated PVDF-HFP and blend_70-30; these data are used to determine the activation energy (**Figure 2b**). Detailed electrochemical impedance spectroscopy (EIS) results for each membrane are provided in **Figure S6**. At every temperature tested, the blend_70-30 QSPE outperforms the pristine_100 QSPE; its conductivity equals or even exceeds that of conventional LEs [29]. The improvement stems from the blend’s optimized amorphous fraction: incorporation of PEG-

PPG-PEG disrupts PVDF-HFP crystalline domains, creating additional pathways for ion transport. Blend_70-30 QSPE follows Arrhenius behavior typical of LEs [30] with activation energy for ion conduction of 0.12 eV, whereas pristine PVDF-HFP exhibits a higher activation energy (0.169 eV), reflecting slower Na^+ kinetics in the pristine QSPE.

The mechanical properties of a QSPE are critical because they influence both dendrite growth and its suppression [31]. Stress-strain tests were performed according to ASTM D882 (**Figure 2c**). The blend_70-30 shows a tensile modulus ($E_{t\text{-}mod}$) of 24.48 MPa nearly twice that of pristine_100 (13.40 MPa), indicating higher resistance to deformation. Its elongation at break, a measure of the ability to deform plastically before fracturing, reaches 114%, whereas the pristine_100 fails at 66%. The ultimate tensile strength likewise rises from 3.55 MPa (pristine_100) to 4.85 MPa (blend_70-30). Incorporating 30 wt.% PEG-PPG-PEG thus enhances both flexibility and modulus, enabling the membrane to withstand the tension stresses generated by dendritic growth and thereby supporting safer, longer-lived battery operation [31]. Optical photographs illustrating the blend_70-30 membrane's flexibility and integrity are provided in **Figure S7.**

Thermal stability was evaluated by thermogravimetric-differential thermogravimetric (TGA-DTG) analysis. The pristine_100 shows a single, sharp weight loss down to 30% at 420 °C (**Figure 2d**), consistent with the known thermal decomposition of PVDF-HFP via chain scission and elimination reactions at 400-450 °C [24,32]. By contrast, the blend_70-30 exhibits a two-step degradation profile (**Figure 2e**). The first step, a 30% weight loss at 350 °C, corresponds to oxidative and random scission of the ether bonds in PEG-PPG-PEG, reported to commence at 300-360 °C [33,34]. The second step, above 400 °C, marks the onset of PVDF-HFP degradation. Incorporation of PEG-PPG-PEG acting as a plasticizer and reducing crystallinity (as confirmed by XRD) slightly lowers the degradation temperature of PVDF-HFP by disrupting its semicrystalline structure and thus reducing the activation energy for thermal decomposition. DTG traces corroborate this shift. In both membranes, the 30% residue is attributed to fluorinated char and other thermally stable species. Moreover, the absence of any weight loss near 80-120 °C indicates negligible moisture or volatile content, confirming the membranes' compatibility with sodium anode and suitability for SMB operation.

Thermal transitions of the polymer membranes were evaluated by differential scanning calorimetry (DSC) analysis. Introducing PEG-PPG-PEG lowers the glass-transition temperature (T_g) from 63.4 °C to 22.5 °C (**Figure 2f**), indicating greater chain flexibility and, in turn, improved ionic transport. The blend_70-30 also exhibits a lower melting temperature (T_m) than the pristine_100, signifying the disruption of crystalline domains [35]. In addition to the degree of crystallinity from the XRD patterns, we also quantified the degree of crystallinity from DSC by integrating the melting endotherm to obtain the melting enthalpy (ΔH_m) [32]. Using the ideal heat of fusion for fully crystalline PVDF-HFP ($\Delta H_m{}^{o}$= 104.7 J g^{-1}) [32], the degree of crystallinity (X_{DSC}, %) was calculated as:

$$X_{DSC} = \frac{\Delta H_m}{\Delta H_m{}^{0}} \times \frac{1}{W_f} \times 100$$

where W_f is the weight fraction of PVDF-HFP in the blend samples.

The pristine_100 exhibits a ΔH_m of 53.6 J g^{-1}, corresponding to a crystallinity of 51%. In contrast, the blend_70-30 membrane shows a ΔH_m of 19.08 J g^{-1}; after normalizing to the 70 wt.% PVDF-HFP content, its crystallinity is 26%. This pronounced reduction highlights the disruptive influence of PEG-PPG-PEG on PVDF-HFP crystallization, most likely through steric hindrance and plasticization by the flexible triblock chains.

In conclusion, the blend_70-30 system featuring robust thermo-mechanical properties, an interconnected porous network, and high ionic conductivity supports a uniform, high Na^+ flux, promotes even sodium deposition, and thus suppresses dendrite growth. A schematic of the QSPEs and their integration into an SMB with Prussian blue (PB) cathode is shown in **Figure 2g**.

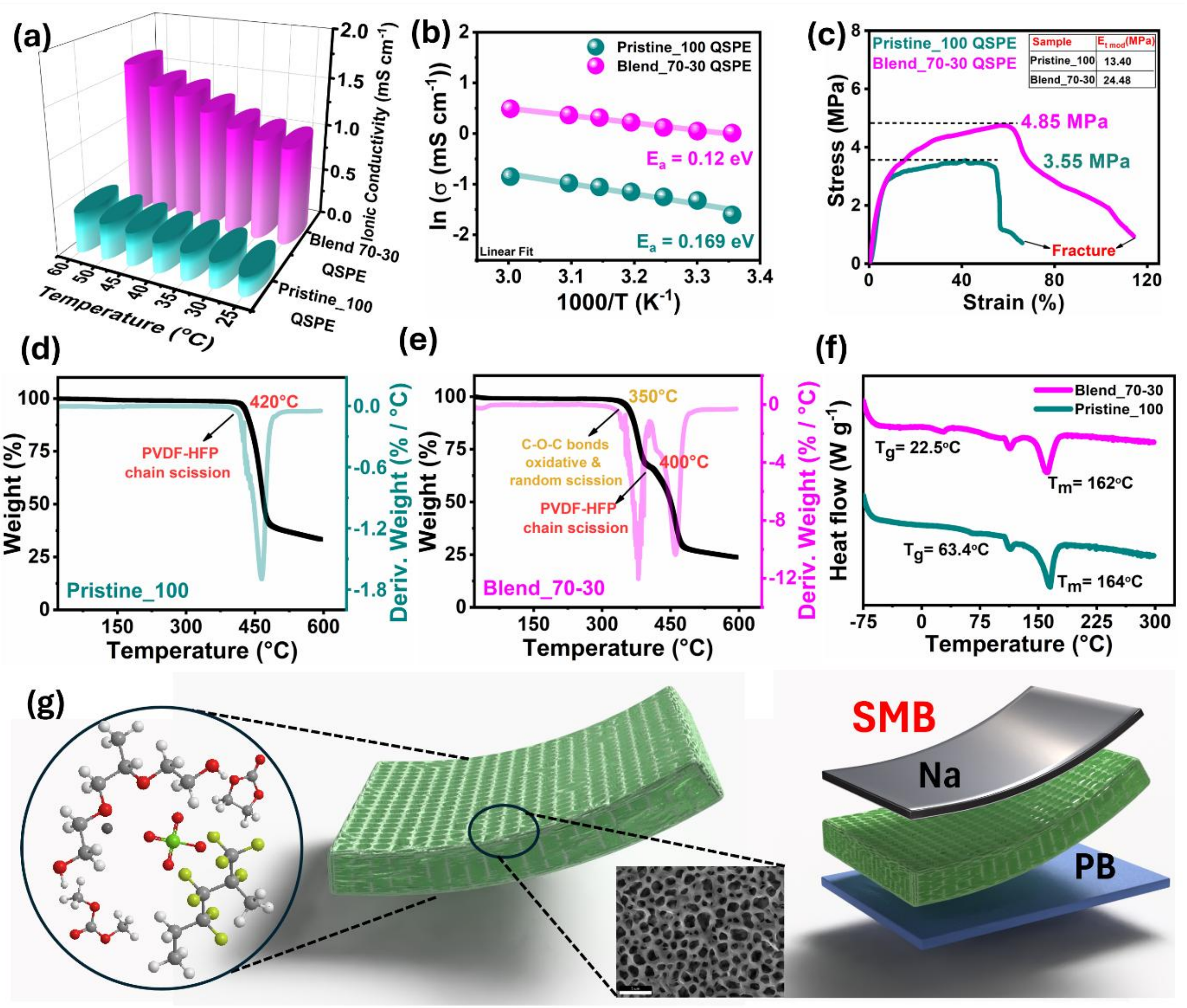

Figure 2. (a) Temperature-dependent ionic conductivities and (b) corresponding Arrhenius plots for pristine_100 and blend_70-30 QSPEs. (c) Room-temperature stress-strain curves of pristine_100 and blend_70-30. (d,e) TGA-DTG profiles of (d) pristine_100 and (e) blend_70-30. (f) DSC thermograms showing T_g and T_m for pristine_100 and blend_70-30. (g) Schematic illustration of the developed QSPE and its integration into an SMB with a PB cathode.

2.3 Solvation properties

Electron-withdrawing groups enhance the solubility of positively charged cations by inducing local dipoles that promote Na^+ dissociation and lower the energy barrier for ion migration [36]. The strong electron-withdrawing $-CF_2$ moieties in PVDF-HFP is further activated by the ester group (-C-O-C-) of PEG-PPG-PEG [37], improving Na-salt solubility in the blend_70-30 QSPE. FTIR spectra of blend_70-30 and pristine_100 QSPEs, together with the $NaClO_4$-based LE, are compared in **Figure 3a**. In the blend_70-30 QSPE, the carbonyl stretching band (-C=O-)

shifts to lower wavenumbers, whereas the -C-O- band moves to higher wavenumbers, indicating specific host-electrolyte interactions [18]. In contrast, the pristine_100 QSPE lacks the carbonyl band and shows a much weaker -C-O- band, signifying minimal interaction with the LE. Owing to the high electronegativity of the -CF and ester groups illustrated schematically in **Figure 3b** the blend_70-30 QSPE becomes transparent after LE activation (**Figure 3c**).

Raman spectroscopy was employed to verify the chemical interactions between the blend_70-30 matrix and the LE (**Figure 3d**). The carbonyl-stretching band (-C=O-) at 715 cm^{-1} [18] prominent in the neat LE remains visible in the blend_70-30 QSPE but is absent in pristine_100 QSPE, confirming that the blend_70-30 QSPE retains the electrolyte's local chemistry. Spectral deconvolution of the 715 cm^{-1} band in the blend_70-30 QSPE reveals that AGGs constitute 54% of the species a substantial increase relative to the LE (**Figure 3e,f**). Conversely, the proportion of contact ion pairs (CIPs) is lower than in the LE. A larger AGG population signifies lower local polarity, which can widen the ESW and improve voltage tolerance [18,38,39]. Moreover, the accompanying increase in anion concentration favors the formation of an inorganic-rich, stable SEI [38,40].

QSPEs combine high ionic conductivity with a broader ESW, giving them a clear advantage over conventional LEs and offering scalability. In this study, pristine_100 and blend_70-30 QSPEs display comparable reduction stability, but the blend_70-30 QSPE shows superior oxidative stability, sustaining an ESW of about 5 V (**Figure 3g**). Electron-withdrawing groups typically enhance oxidative resistance by lowering the electron density of the polymer backbone [18,23]. Accordingly, the pristine_100 matrix, which contains more electron-withdrawing segments, exhibits a higher oxidation current, whereas the -C-O-C- groups in PEG-PPG-PEG moderate the local electronic environment, improving the oxidation stability of blend_70-30. The wider ESW also aligns with solvation effects: the higher content of AGG in blend_70-30 increases anion concentration and reduces local polarity, both of which are known to extend the ESW [18,39,40]. Consequently, the QSPEs containing -C-O-C- groups exhibit ESW above 4.8 V (**Figure S8**).

Chronoamperometry was employed to determine the Na^+ transference number, which was calculated with the Bruce-Vincent method [14,31]. As shown in **Figure 3i**, the blend_70-30 QSPE displaying a room-temperature ionic conductivity of 1.01 mS cm^{-1} achieves a Na^+ transference number of 0.78, essentially matching that of the LE [15,41]. By contrast, pristine_100 QSPE shows a lower transference number of 0.65 (**Figure 3h**). The high value confirms efficient salt dissociation within the blend_70-30 matrix.

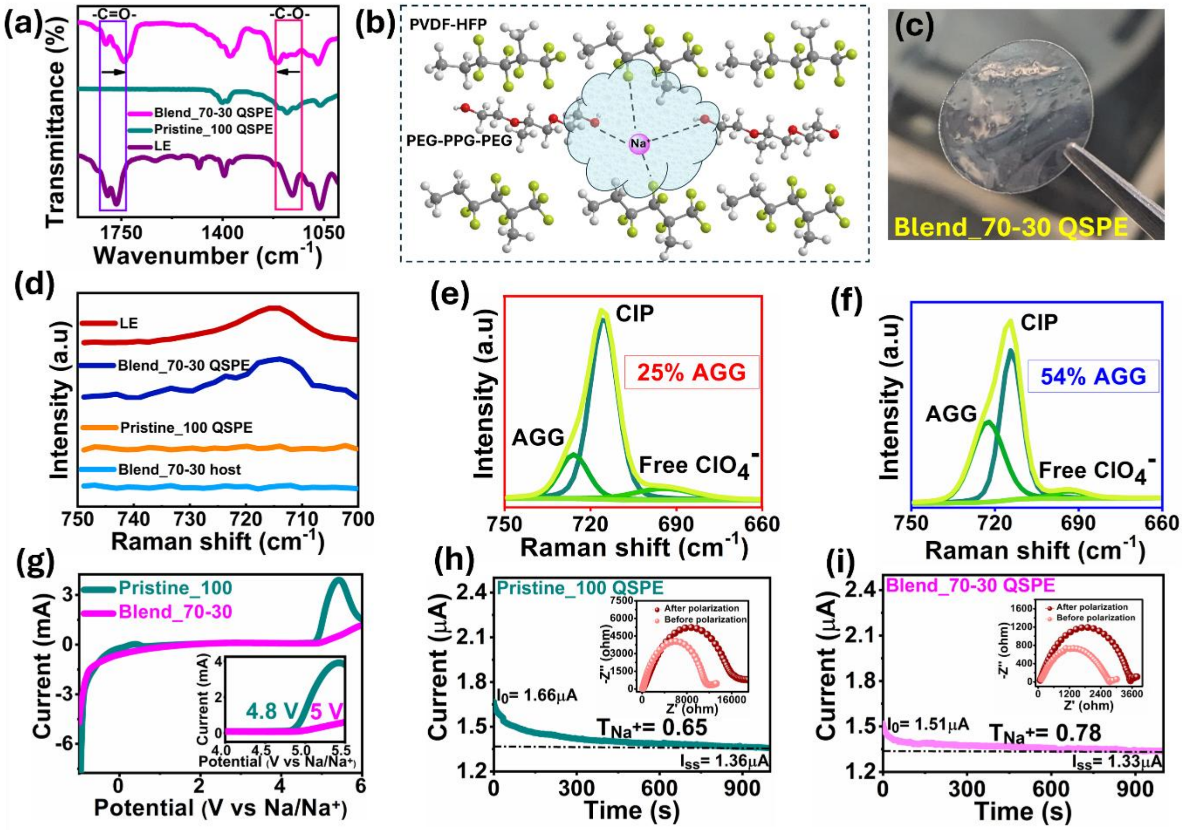

Figure 3. (a) FTIR spectra of the LE and QSPEs. (b) Schematic illustration of sodium-ion interaction with the blend_70-30 matrix. (c) Photograph of the blend_70-30 QSPE. (d) Raman spectra of the blend_70-30 host, pristine_100 QSPE, blend_70-30 QSPE, and LE. (e,f) Deconvoluted Raman spectra of (e) LE and (f) blend_70-30 QSPE. (g) Linear sweep voltammetry showing the ESW of pristine_100 and blend_70-30 QSPEs (inset: magnified curve from 4.0 to 5.5 V). (h,i) Chronoamperometry of Na//pristne_100 QSPE//Na and Na//blend_70-30 QSPE//Na cells (inset: AC impedance spectra before and after polarization).

2.4 Computational

2.4.1 DFT Calculations

Theoretical calculations were performed to elucidate the contributions of solvent molecules, polymeric macromolecules, and Na salt to the formation of the SEI. The electronic structures of EC, FEC, DMC, PVDF-HFP, PEG-PPG-PEG, and NaClO$_4$ were calculated using DFT as implemented in the ONETEP program[42,43]. A kinetic energy cutoff of 1000.0 eV was used for the basis set, which consists of psinc functions equivalent to plane waves[44]. The orbitals are represented using non-orthogonal generalized Wannier functions with a localization radius of 10.0 a_0[45]. The Perdew-Burke-Ernzerhof (PBE) generalized gradient approximation was used for the exchange-correlation functional. The shapes and energy levels of the highest occupied molecular orbital (HOMO) and the lowest unoccupied molecular orbital are shown in **Figure 4a**. The presence of fluorinated groups in FEC lowers its LUMO energy compared to EC. Similarly, the fluorine groups in PVDF-HFP reduce its LUMO energy level. A lower LUMO energy increases the likelihood of reduction at the Na metal anode. The reduction of these fluorinated species is expected to produce fluoride-rich products, passivating further reactions, stabilizing the SEI, and suppressing dendrite growth. Thus, combining solvation structure analysis with theoretical calculations suggests that the SEI will be predominantly composed of inorganic species, which should contribute to longer cycle life in SMBs.

Overall, DFT calculations reveal that the electron-withdrawing fluorine atoms in FEC and PVDF-HFP lower the LUMO levels compared to their non-fluorinated counterparts. This lowering of the LUMO promotes the reductive decomposition of FEC and PVDF-HFP at the sodium metal surface, facilitating the formation of a robust, stable, fluoride-rich SEI that passivates further electrolyte degradation and mitigates dendrite formation. Moreover, the increased concentration of AGGs induced by PEG-PPG-PEG widens the ESW and contributes additional inorganic components to the SEI through the decomposition of salt anions [38].

2.4.2 MD simulations

To gain further insights into the solvation structure, MD simulations of the electrolyte system were performed using the Multi-Atomic Cluster Expansion (MACE) force field [46]. To replicate the experimental composition of blend_70-30 QSPE, a periodic simulation cell (25.0 Å) was constructed using PACKMOL software [47], containing 7 EC, 2 FEC, 5 DMC, 44 PVDF-HFP, 20 PEG-PPG-PEG, and 2 $NaClO_4$, totaling 1714 atoms. Geometry optimization was first carried out until all forces fell below 0.05 eV $Å^{-1}$. MD simulations were then performed in the NVT ensemble (number of particles (N), volume (V), and temperature (T) were kept constant) using a Langevin thermostat at 300 K. The temperature and total energy profiles during the MD simulation are shown in **Figure S9**, indicating that the system reaches equilibrium after 100 ps. A snapshot of the equilibrated structure at 100 ps is shown in **Figure 4b**, along with a zoomed-in view of the salt coordination environment. Na^+ cations are found to coordinate predominantly with the fluorine atoms of the PVDF-HFP polymer chains, while one Na^+ cation also coordinates with the carbonyl oxygen of an EC molecule in the solvent. Another Na^+ cation is surrounded by ClO_4^- anions within its solvation shell, forming an AGG.

Transport properties of complex polymeric electrolytes can be calculated from the Onsager transport coefficients, which generally decrease with increasing polymer chain length in simulations [48]. Here, monomeric units of PVDF-HFP and PEG-PPG-PEG were used in MD simulations. As a result, the computed transport properties may represent an upper bound relative to those achievable in practical polymeric systems. The methodology for calculating diffusion coefficients, ionic conductivity, and transference numbers is detailed in the Supplementary Information (Section 2.1). Diffusion coefficients were obtained from the slopes of the mean squared displacement plots for Na^+ and ClO_4^- ions, as shown in **Figure S10**. Theoretical calculations yield diffusion coefficients of 2.57×10^{-6} cm^2 s^{-1} for Na^+ and 3.41×10^{-7} cm^2 s^{-1} for ClO_4^-, along with a total ionic conductivity of 2.10 mS cm^{-1}. These values support the experimentally observed high performance of the blend_70-30 QSPE. The computed Na^+ transference number of 0.90 further underscores the capability for efficient ion transport in the blend_70-30 QSPE. These predictions are consistent with the typical overestimations associated with MD simulations using short-chain polymers. Collectively, these multiscale computational and experimental insights highlight the pivotal role of electron-withdrawing groups and fluorinated components in modeling solvation characteristics, stabilizing interphases, and promoting efficient ion transport in SMBs.

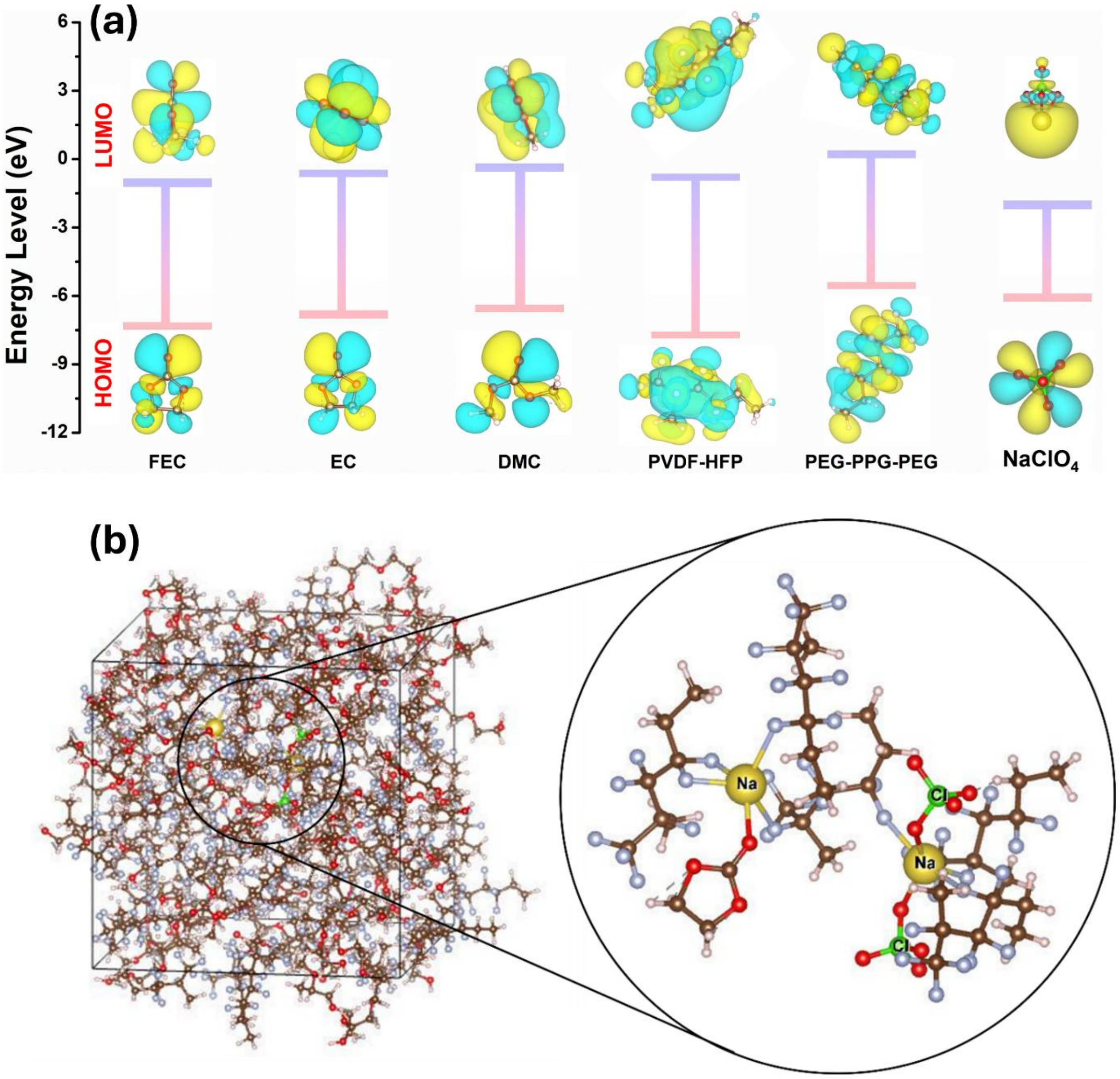

Figure 4. (a) Molecular orbital shapes and energy levels of the HOMO and LUMO for FEC, EC, DMC, PVDF-HFP, PEG-PPG-PEG, and NaClO$_4$. (b) Snapshot of the electrolyte system from MD simulations after 100 ps.

2.5 Electrochemical properties

Since solvation properties directly influence electrochemical behavior, further investigations were carried out in this regard. Galvanostatic stripping/plating of Na was evaluated using Na//Na symmetric cells assembled with the blend_70-30 QSPE, with a symmetric cell based on the pristine_100 QSPE also tested for comparison. The cell with the blend_70-30 QSPE, benefitting from the electron-donating -C-O-C- groups of PEG-PPG-PEG, exhibits lower local polarity and superior solvation effects, resulting in a lower deposition overpotential compared to the cell with the pristine_100 QSPE (**Figure 5a-d**). The stripping/plating overpotential for blend_70-30 QSPE cell is approximately 250 mV with a uniform and stable profile (**Figure 5c, d**), significantly lower than that of the pristine_100 QSPE cell (~350 mV). While the pristine_100 QSPE cell initially shows a lower overpotential, it suffers from short-circuiting within 75 hours, likely due to the non-uniform deposition of Na leading to dendrite formation [38,49]. Furthermore, the lower AGG concentration in the pristine_100 cell likely results in the formation of an organic-rich SEI [18], accelerating dendrite growth and correlating with the unstable stripping/plating behavior (**Figure 5a,b**). Overall, galvanostatic stripping/plating analyses indicate that the blend_70-30 QSPE cell more effectively suppresses Na dendrite formation compared to the pristine_100 QSPE cell.

To investigate the kinetics of Na^+ stripping/plating, Tafel plots were obtained using Na//Na symmetric cells assembled with pristine_100 and blend_70-30 QSPEs. As shown in **Figure 5e**, the blend QSPE exhibits an exchange current density of 0.0165 mA cm^{-2}, whereas the pristine_100 QSPE shows a significantly lower value of 0.003 mA cm^{-2}. Notably, a higher exchange current density indicates reduced Na^+ nucleation barriers during the electrodeposition process [50]. The fivefold enhancement in exchange current density for the blend_70-30 QSPE reflects improved charge-transfer kinetics at the Na electrode-electrolyte interface, which can be correlated with the formation of a highly conductive and stable inorganic-rich SEI [51]. Post-mortem morphological analysis by FESEM was further conducted to correlate the observations from overpotential measurements, exchange current densities, and Na deposition behavior after 10 galvanostatic cycles. As anticipated from the solvation characteristics and the galvanostatic plating/stripping profiles, the pristine_100 QSPE exhibits non-uniform Na deposition, with visible fractures and roughness (**Figure 5f**). Such porous and irregular Na surfaces can degrade electrochemical performance and pose serious safety risks during battery operation [52]. In contrast, the blend_70-30 QSPE exhibits a smoother, denser Na deposition morphology (**Figure 5g**). Schematic representations of the interfacial structures formed on Na metal are shown in **Figure 5h, i**. As ionic transport across the QSPE-electrode interface is governed by the functional groups of the polymer host, the synergistic effects of the fluorine groups from PVDF-HFP and -C-O-C- groups from PEG-PPG-PEG promote enhanced ionic conductivity and enable uniform Na deposition, thereby ensuring a stable and robust interface.

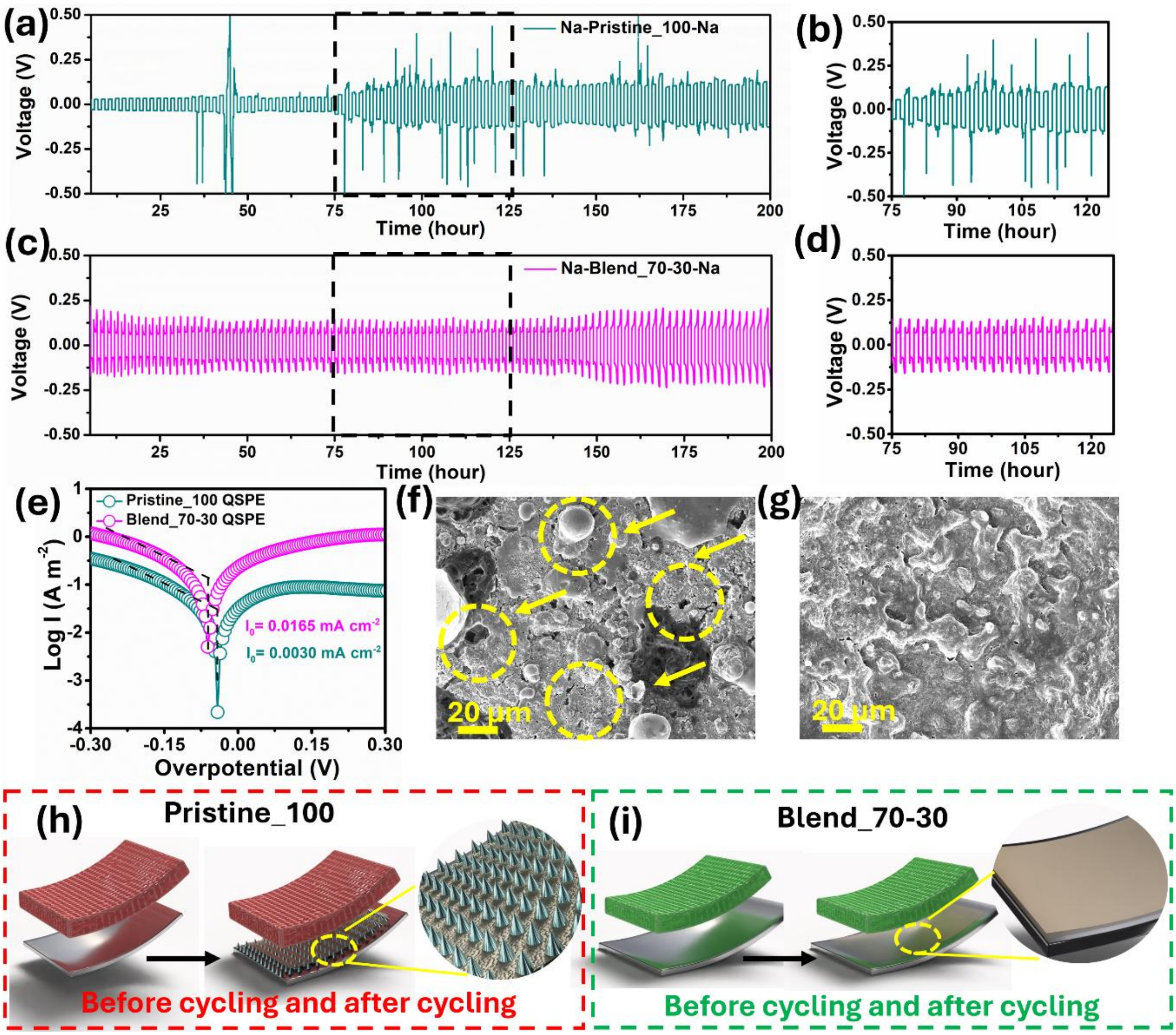

Figure 5. (a-d) Galvanostatic cycling performance of Na symmetric cells using (a,b) pristne_100 and (c,d) blend_70-30 QSPEs at 1 mA cm^{-2} (e) Overlaid Tafel curves of Na symmetric cells with pristne_100 and blend_70-30 QSPEs. (f,g) SEM images of post-cycled sodium metal electrodes after 10 cycles at 1 mA cm^{-2} for cells with (f) pristine_100 and (g) blend_70-30 QSPEs. (h,i) Schematic representations of the Na metal interface before and after cycling with the respective QSPEs.

To experimentally validate the implications of the solvation analysis and theoretical results, the chemical nature of the Na metal anode interface was investigated by X-ray photoelectron spectroscopy (XPS) [53,54]. XPS measurements were conducted on the surface of cycled sodium after 10 cycles at 1 mA cm^{-2} in Na//Na symmetric cells employing pristine_100 and blend_70-30 QSPEs to assess the SEI composition. For the pristine_100 QSPE cell, the high-resolution C1s spectrum reveals typical electrolyte decomposition products, with peaks at 284.8 eV (–C–C–), 286.2 eV (C=O), and broad bands at 288.0 and 290.0 eV (O-C=O) generated during cycling (**Figure 6a**) [38,55]. The weak oxyfluoride (-O-F) peak observed in the O 1s spectrum suggests the decomposition of the FEC additive (**Figure 6b**). Deconvolution of the Na 1s, F 1s, and Cl 2p peaks further confirms the presence of inorganic components within the SEI (**Figure 6c-e**). In contrast, the blend_70-30 QSPE cell exhibits significantly higher relative intensities for NaF, Na_2CO_3, NaO, and NaCl, indicating the formation of an inorganic-rich SEI (**Figure 6f-j**).

It is well established that a stable, inorganic-rich SEI serves as a protective barrier, inhibiting parasitic reactions and suppressing dendritic growth [56]. This is further corroborated by the Cl 2p spectra observed for both the pristine_100 and the blend_70-30 QSPEs. The anionic species, perchlorate (ClO_4^-), preferentially deposits on the Na metal surface, forming a NaCl-rich interphase that protects the electrode and suppresses side reactions. Overall, the formation of an inorganic-rich SEI characterized by high concentrations of NaF, Na_2CO_3, and NaCl correlates with the reduced overpotentials and stable voltage profiles observed during galvanostatic cycling of the blend_70-30 QSPE cell. These XPS results validate the mechanistic insights gained from solvation analysis and theoretical calculations, revealing the origin of the improved electrochemical performance of cells cycled with the blend_70-30 QSPE. Moreover, these findings highlight the synergistic effect of fluorinated groups in PVDF-HFP and the electron-donating -C-O-C- groups in PEG-PPG-PEG in enhancing the interfacial stability and overall performance of Na metal anodes.

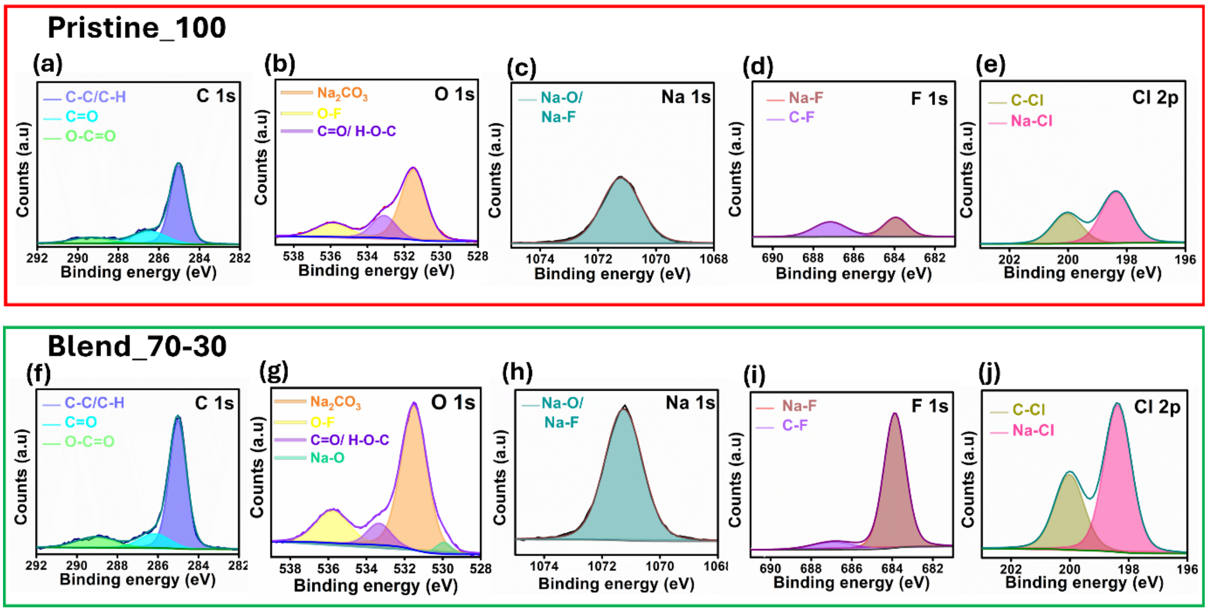

Figure 6. High-resolution XPS spectra of (a,f) C 1s, (b,g) O 1s, (c,h) Na 1s, (d,i) F 1s, and (e,j) Cl 2p for sodium metal electrodes in the stripped state, using QSPEs based on (a-e) pristine_100 and (f-j) blend_70-30, respectively.

Based on fundamental studies of ionic conductivity, solvation characteristics, transference number, exchange current density, and overall electrochemical performance, the blend_70-30 QSPE exhibits properties comparable to those of a LE. Accordingly, it is hereafter referred to as a liquid-like QSPE (L-QSPE). To evaluate the practical applicability of the developed L-QSPE, a full cell comprising a Prussian blue analogue (PB) cathode and a Na metal anode was assembled. The detailed PB synthesis procedure, along with its material characterization and electrode fabrication, is provided in the Supplementary Information (**Figure S11**) [31,57].

The Na//L-QSPE//PB cells deliver an initial capacity of 159 mAh g^{-1} at 0.5 C (**Figure 7b**). For comparison, a full cell using the pristine_100 QSPE was also tested (**Figure 7a**). Notably, the charge-discharge plateaus observed for the PB cathode align well with the cyclic voltammetry (CV) curves, showing corresponding oxidation and reduction peaks (**Figure S12**). To further examine the evolution of interfacial resistance during cycling, EIS was conducted on the Na//L-QSPE//PB cell at various stages (**Figure 7c**). Prior to cycling, the interfacial resistance is approximately 185 Ω, which decreases to 105 Ω after 10 cycles and further to ~5 Ω after 50 cycles. This progressive decrease in interfacial resistance suggests interfacial activation, consistent with the formation of a stable, inorganic-rich SEI as predicted by theoretical calculation and confirmed by XPS analysis.

Rate performance and capacity recovery at various C-rates were also evaluated for both cells (**Figure 7d**). Compared to the pristine_100 QSPE cell, the L-QSPE cell exhibits superior reversible capacity retention. In contrast, the pristine_100 QSPE cell fails to recover its initial capacity and displays a steadily declining profile. Long-term cycling performance at 0.5 C further highlights this difference (**Figure 7e**): the pristine_100 QSPE cell completely fails after 200 cycles, whereas the L-QSPE cell sustains stable operation for over 500 cycles, maintaining an average Coulombic efficiency (CE) of ~ 98%.

To assess safety, a flame test was performed, with the corresponding optical images presented in **Figure S13**. Compared to commercial LE-soaked Celgard separators, the L-QSPE exhibits delayed fire propagation and self-extinguishing behavior. This improved flame retardancy is attributed to the presence of halogenated compounds, particularly fluorine atoms embedded within the polymer matrix, which suppress combustion. Additionally, the immobilization of LE within the QSPE matrix reduces the concentration of low-flash-point volatile solvents [58], thereby mitigating flammability risks. This effect is further amplified by the inclusion of the fluorinated FEC additive. A comparison table summarizing the performance of the developed L-QSPE relative to reported systems (**Table S1**) demonstrates its superior electrochemical and safety characteristics. These findings emphasize the effectiveness of optimizing polymer blend compositions, engineering solvation environments, and tailoring SEI formation to achieve high-performance solid polymer batteries.

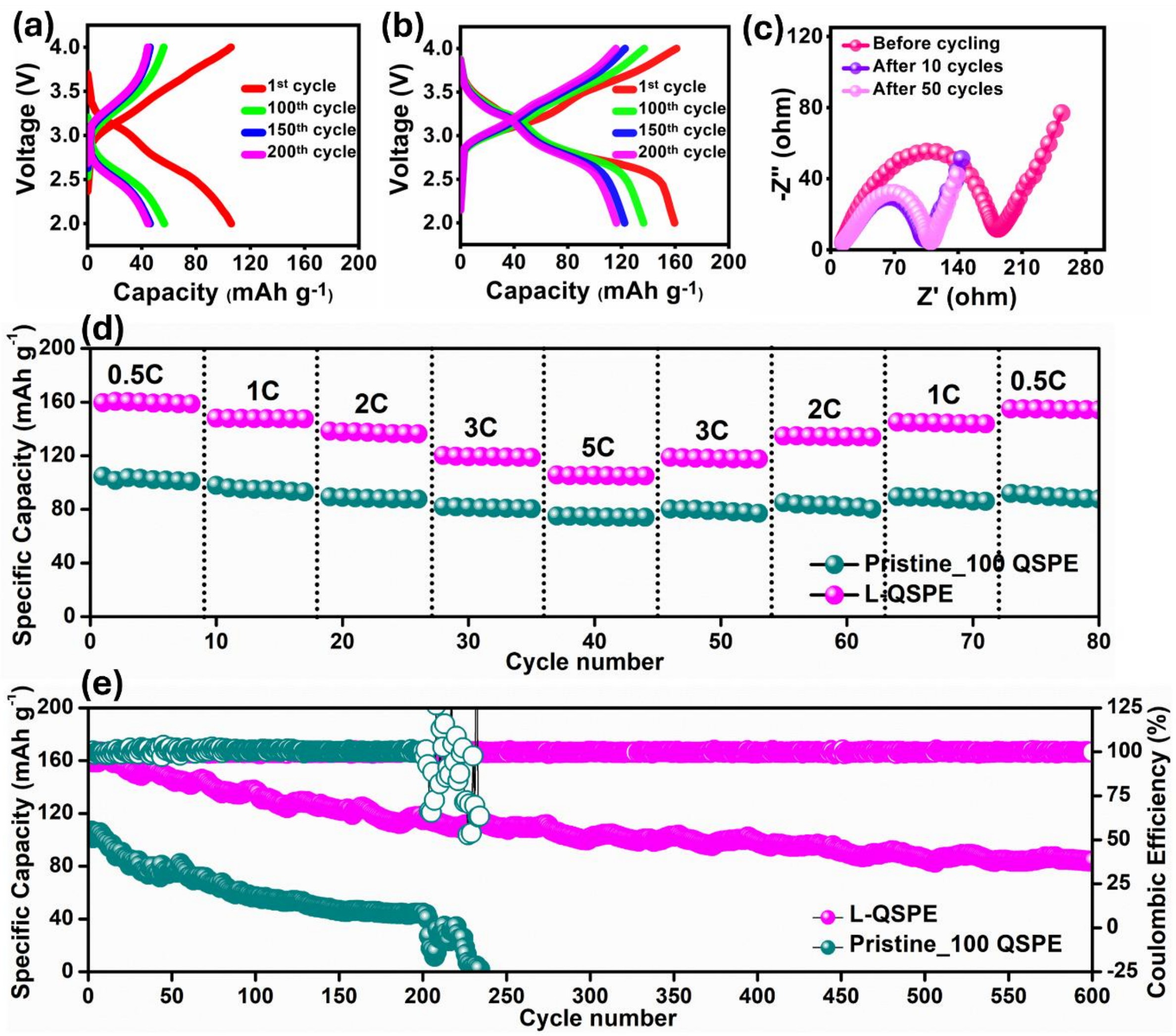

Figure 7. (a,b) Galvanostatic charge-discharge curves of Na//QSPE//PB cells using (a) pristine_100 QSPE and (b) L-QSPE, cycled at 0.5 C. (c) EIS spectra of the Na//L-QSPE//PB cell recorded after various cycles at 0.5 C. (d) Reversible rate performance of the cells cycled from 0.5 C to 5 C and vice-versa. (e) Long-term cycling performance at 0.5 C for cells based on pristine_100 QSPE and L-QSPE. All tests were performed under ambient conditions.

3. Conclusions

In summary, a highly ionically conductive and thermomechanically stable QSPE mimicking a “liquid-like” system has been successfully fabricated for high-performance SMBs. The optimized L-QSPE exhibits an ionic conductivity of 1.01 mS cm^{-1} and an activation energy of 0.12 eV, comparable to that of liquid electrolytes. Incorporation of the PEG-PPG-PEG molecule enhances the amorphous nature and promotes the formation of an interconnected porous network, enabling high electrolyte uptake (240 %) and porosity (72 %). The presence of -C-O-C- groups facilitates a favorable solvation environment, supporting the formation of AGGs. Coupled with excellent mechanical properties, the L-QSPE delivers a stable Na plating/stripping profile for over 200 h with a low overpotential (250 mV), and a high exchange current density of 0.0165 mA cm^{-2}, indicating improved Na nucleation and growth kinetics. A high Na^{+} transference number of 0.78 and the elevated AGG content correlate with an expanded ESW, attributed to reduced local polarity via the solvation effect. DFT calculations reveal that fluorinated groups in PVDF-HFP lower the LUMO energy level, which enhances reduction propensity at the Na metal surface. The resulting fluoride-based SEI products passivate further reactions, stabilizing the interface and mitigating degradation. MD simulations further highlight the role of electron-withdrawing groups in engineering solvation structures and enhancing ionic transport of L-QSPE, predicting an ionic conductivity of 2.10 mS cm^{-1} and a transference number of 0.90 consistent with experimental observations. Finally, a Na//L-QSPE//PB full cell demonstrates excellent cycling stability, maintaining an average CE of 98% over 500 cycles at 0.5 C. These results underscore the potential of L-QSPE to drive the development of next-generation QSPE-based high-performance SMB systems.

4. Acknowledgement

We would like to thank IIT-Delhi, India, and UQ, Australia, for the collaborative program, UQIDAR, for the support throughout this work. The authors acknowledge the central research facility (CRF), IIT-Delhi, India, for the usage of various analytical facilities. The authors thank IIT Delhi HPC facility for computational resources. A.B. acknowledges seed grant from IIT Delhi (SGNF148). This work was partially supported by the UQ-Yonsei International Research Program, the JST-ERATO Yamauchi Materials Space Tectonics Project (JPMJER2003), and the ARC Laureate Fellowship (FL230100095). M. H thanks the support from JSPS Postdoctoral Fellowships for Research in Japan. This work used the Queensland node of the NCRIS-enabled Australian National Fabrication Facility (ANFF).

During the preparation of this work, the authors used ChatGPT to check English grammar. After using this tool, the authors reviewed and edited the content as needed and take full responsibility for the content of the publication.

5. Declaration of interest

The authors declare no conflict of interest.

6. Reference

1 C. Bao, B. Wang, P. Liu, H. Wu, Y. Zhou, D. Wang, H. Liu and S. Dou, *Adv. Funct. Mater.*, 2020, **30**, 2004891.

2 Y. Zhao, X. Yang, L.-Y. Kuo, P. Kaghazchi, Q. Sun, J. Liang, B. Wang, A. Lushington, R. Li, H. Zhang and X. Sun, *Small*, 2018, **14**, 1703717.

3 T. Liu, X. Yang, J. Nai, Y. Wang, Y. Liu, C. Liu and X. Tao, *Chem. Eng. J.*, 2021, **409**, 127943.

4 G. G. Eshetu, G. A. Elia, M. Armand, M. Forsyth, S. Komaba, T. Rojo and S. Passerini, *Adv. Energy Mater.*, 2020, **10**, 2000093.

5 J. Lee, J. Kim, S. Kim, C. Jo and J. Lee, *Mater. Adv.*, 2020, **1**, 3143–3166.

6 C. Yan, R. Xu, Y. Xiao, J. Ding, L. Xu, B. Li and J. Huang, *Adv. Funct. Mater.*, 2020, **30**, 1909887.

7 A. M. Tripathi, W.-N. Su and B. J. Hwang, *Chem. Soc. Rev.*, 2018, **47**, 736–851.

8 S. K. Vineeth and V. Kumar, in *Room-temperature Sodium-Sulfur Batteries*, CRC Press, Boca Raton, 2023, pp. 1–16.

9 S. K. Vineeth, C. B. Soni, Y. Sun, V. Kumar and Z. W. Seh, *Trends Chem.*, 2022, **4**, 48–59.

10 S. Wang, Y. Chen, Y. Jie, S. Lang, J. Song, Z. Lei, S. Wang, X. Ren, D. Wang, X. Li, R. Cao, G. Zhang and S. Jiao, *Small Methods*, 2020, **4**, 1900856.

11 T. Wang, Y. Hua, Z. Xu and J. S. Yu, *Small*, 2022, **18**, 2102250.

12 G. Xi, M. Xiao, S. Wang, D. Han, Y. Li and Y. Meng, *Adv. Funct. Mater.*, 2021, **31**, 2007598.

13 S. K. Vineeth, M. Tebyetekerwa, H. Liu, C. B. Soni, Sungjemmenla, X. S. Zhao and V. Kumar, *Mater. Adv.*, 2022, **3**, 6415–6440.

14 G. Chen, K. Zhang, Y. Liu, L. Ye, Y. Gao, W. Lin, H. Xu, X. Wang, Y. Bai and C. Wu, *Chem. Eng. J.*, 2020, **401**, 126065.

15 S. K. Vineeth, Sungjemmenla, Y. Yamauchi and V. Kumar, in *Room-temperature Sodium-Sulfur Batteries*, CRC Press, Boca Raton, 1st edn., 2023, pp. 79–114.

16 C. Luo, T. Shen, H. Ji, D. Huang, J. Liu, B. Ke, Y. Wu, Y. Chen and C. Yan, *Small*, 2020, **16**, 1906208.

17 Q. Zeng, D. Zhu, J. Shan, Q. Gao, J. Xu, Q. Xu, P. Shi and Y. Min, *Chem. Eng. J.*, 2024, **486**, 150189.

18 Y. Zhang, H. Lai, X. Wu and Z. Wen, *Small Methods*, 2024, **2400280**, 1–10.

19 Y. Shuai, J. Lou, X. Pei, C. Su, X. Ye, L. Zhang, Y. Wang, Z. Xu, P. Gao, S. He, Z. Wang and K. Chen, *ACS Appl. Mater. Interfaces*, 2022, **14**, 45382–45391.

20 D. Wang, H. Xie, Q. Liu, K. Mu, Z. Song, W. Xu, L. Tian, C. Zhu and J. Xu, *Angew. Chemie Int. Ed.*, , DOI:10.1002/anie.202302767.

21 S. K. Vineeth, P. Sreeram, A. Vlad, R. Joy, P. Raghavan and A. Pullanchiyodan, in *Polymer Blend Nanocomposites for Energy Storage Applications*, Elsevier, 2023, pp. 203–238.

22 W. Zhang, J. Zhang, X. Liu, H. Li, Y. Guo, C. Geng, Y. Tao and Q. Yang, *Adv. Funct. Mater.*, 2022, **32**, 2201205.

23 F. Gebert, J. Knott, R. Gorkin, S.-L. Chou and S.-X. Dou, *Energy Storage Mater.*, 2021, **36**, 10–30.

24 N. S. Jishnu, S. K. Vineeth, A. Das, N. T. M. Balakrishnan, A. P. Thomas, M. J. Jabeen Fatima, J.-H. Ahn and R. Prasanth, in *Electrospinning for Advanced Energy Storage Applications*, eds. N. T. M. Balakrishnan and R. Prasanth, Springer Singapore, Singapore, 1st edn., 2021, pp. 201–234.

25 C. Wunder, T.-L. Lai, E. Šić, T. Gutmann, E. De Vito, G. Buntkowsky, M. Zarrabeitia and S. Passerini, *J. Mater. Chem. A*, 2024, **12**, 20935–20946.

26 D. T. Vo, H. N. Do, T. T. Nguyen, T. T. H. Nguyen, V. M. Tran, S. Okada and M. L. P. Le, *Mater. Sci. Eng. B*, 2019, **241**, 27–35.

27 L. Yi, C. Zou, X. Chen, J. Liu, S. Cao, X. Tao, Z. Zang, L. Liu, B. Chang, Y. Shen and X. Wang, *ACS Appl. Energy Mater.*, 2022, **5**, 7317–7327.

28 N. Wang, D. Qin, Q. Sun, X. Chen, Y. Song and T. Xin, *ACS Appl. Polym. Mater.*, 2023, **5**, 2607–2616.

29 V. Kumar, A. Y. S. Eng, Y. Wang, D.-T. Nguyen, M.-F. Ng and Z. W. Seh, *Energy*

Storage Mater., 2020, **29**, 1–8.

30 J. Lv, Q. Wang, M. OuYang and Y. Cao, *ACS Appl. Mater. Interfaces*, 2024, **16**, 41570–41582.

31 S. K. Vineeth, C. B. Soni, Sungjemmenla, C. Sanjaykumar, Y. Yamauchi, M. Han and V. Kumar, *J. Energy Storage*, 2023, **73**, 108780.

32 Y. Laxmayyaguddi, N. Mydur, A. Shankar Pawar, V. Hebri, M. Vandana, G. Sanjeev and D. Hundekal, *ACS Omega*, 2018, **3**, 14188–14200.

33 D. Saikia, H. Y. Wu, Y. C. Pan, C. P. Lin, K. P. Huang, K. N. Chen, G. T. K. Fey and H. M. Kao, *J. Power Sources*, 2011, **196**, 2826–2834.

34 J. Glastrup, *Polym. Degrad. Stab.*, 2003, **81**, 273–278.

35 Y. Sha, T. Dong, Q. Zhao, H. Zheng, X. Wen, S. Chen and S. Zhang, *Ionics (Kiel).*, 2020, **26**, 4803–4812.

36 J. Wang, P. Kumar, Z. Ma, H. Liang, F. Zhao, H. Xie, Y. Wang, T. Cai, Z. Cao, L. Cavallo, Q. Li and J. Ming, *ACS Energy Lett.*, 2024, **9**, 4386–4398.

37 S. Heng, Y. Wang, Q. Qu, R. Guo, X. Shan, V. S. Battaglia, G. Liu and H. Zheng, *ACS Appl. Energy Mater.*, 2019, **2**, 6404–6416.

38 C. B. Soni, S. Bera, Sungjemmenla, M. Chandra, V. S. K., S. Kumar, H. Kumar and V. Kumar, *J. Mater. Chem. A*, 2024, **12**, 21853–21863.

39 S. Xue, Y. Zhou, Z. Zhang, K. Hou, M. He and X. Liu, *J. Energy Storage*, 2024, **95**, 112558.

40 S. Yao, C. Guo, Y. Yang, X. Liu, J. Wang, J. Geng, H. Li, C. Hong, H. Li, R. Tao, J. Liang and J. Liu, *Adv. Funct. Mater.*, , DOI:10.1002/adfm.202419656.

41 J. Zheng, S. Chen, W. Zhao, J. Song, M. H. Engelhard and J.-G. Zhang, *ACS Energy Lett.*, 2018, **3**, 315–321.

42 J. C. A. Prentice, J. Aarons, J. C. Womack, A. E. A. Allen, L. Andrinopoulos, L. Anton, R. A. Bell, A. Bhandari, G. A. Bramley, R. J. Charlton, R. J. Clements, D. J. Cole, G. Constantinescu, F. Corsetti, S. M. M. Dubois, K. K. B. Duff, J. M. Escartín, A. Greco, Q. Hill, L. P. Lee, E. Linscott, D. D. O'Regan, M. J. S. Phipps, L. E. Ratcliff, Á. R. Serrano, E. W. Tait, G. Teobaldi, V. Vitale, N. Yeung, T. J. Zuehlsdorff, J. Dziedzic, P.

D. Haynes, N. D. M. Hine, A. A. Mostofi, M. C. Payne and C.-K. Skylaris, *J. Chem. Phys.*, , DOI:10.1063/5.0004445.

43 C. K. Skylaris, P. D. Haynes, A. A. Mostofi and M. C. Payne, *J. Chem. Phys.*, , DOI:10.1063/1.1839852.

44 A. A. Mostofi, P. D. Haynes, C.-K. Skylaris and M. C. Payne, *J. Chem. Phys.*, 2003, **119**, 8842–8848.

45 C.-K. Skylaris, A. A. Mostofi, P. D. Haynes, O. Diéguez and M. C. Payne, *Phys. Rev. B*, 2002, **66**, 035119.

46 I. Batatia, P. Benner, Y. Chiang, A. M. Elena, D. P. Kovács, J. Riebesell, X. R. Advincula, M. Asta, M. Avaylon, W. J. Baldwin, F. Berger, N. Bernstein, A. Bhowmik, S. M. Blau, V. Cărare, J. P. Darby, S. De, F. Della Pia, V. L. Deringer, R. Elijošius, Z. El-Machachi, F. Falcioni, E. Fako, A. C. Ferrari, A. Genreith-Schriever, J. George, R. E. A. Goodall, C. P. Grey, P. Grigorev, S. Han, W. Handley, H. H. Heenen, K. Hermansson, C. Holm, J. Jaafar, S. Hofmann, K. S. Jakob, H. Jung, V. Kapil, A. D. Kaplan, N. Karimitari, J. R. Kermode, N. Kroupa, J. Kullgren, M. C. Kuner, D. Kuryla, G. Liepuoniute, J. T. Margraf, I.-B. Magdău, A. Michaelides, J. H. Moore, A. A. Naik, S. P. Niblett, S. W. Norwood, N. O'Neill, C. Ortner, K. A. Persson, K. Reuter, A. S. Rosen, L. L. Schaaf, C. Schran, B. X. Shi, E. Sivonxay, T. K. Stenczel, V. Svahn, C. Sutton, T. D. Swinburne, J. Tilly, C. van der Oord, E. Varga-Umbrich, T. Vegge, M. Vondrák, Y. Wang, W. C. Witt, F. Zills and G. Csányi, , DOI:10.48550/arXiv.2401.00096.

47 L. Martínez, R. Andrade, E. G. Birgin and J. M. Martínez, *J. Comput. Chem.*, 2009, **30**, 2157–2164.

48 K. D. Fong, J. Self, B. D. McCloskey and K. A. Persson, *Macromolecules*, 2020, **53**, 9503–9512.

49 H. Wang, C. Wang, E. Matios and W. Li, *Angew. Chemie*, 2018, **130**, 7860–7863.

50 T. Zhao, X. Zheng, D. Wang, L. Huang, B. Li, X. Liu, H. Yang, Y. Dai, Y. Huang and W. Luo, *Adv. Funct. Mater.*, , DOI:10.1002/adfm.202304928.

51 Z. Piao, P. Xiao, R. Luo, J. Ma, R. Gao, C. Li, J. Tan, K. Yu, G. Zhou and H. M. Cheng, *Adv. Mater.*, 2022, **34**, 1–10.

52 M. Mandl, J. Becherer, D. Kramer, R. Mönig, T. Diemant, R. J. Behm, M. Hahn, O. Böse and M. A. Danzer, *Electrochim. Acta*, 2020, **354**, 136698.

53 C. B. Soni, Sungjemmenla, S. K. Vineeth, C. S. Kumar and V. Kumar, *Sustain. Energy Fuels*, 2023, **7**, 1908–1915.

54 C. B. Soni, S. K. Barik, S. K. Vineeth, B. Yadav, M. Chandra, Sungjemmenla, S. C, H. Kumar and V. Kumar, *J. Mater. Chem. A*, 2025, **13**, 6813–6825.

55 C. B. Soni, S. Bera, Sungjemmenla, S. K. Vineeth, H. Kumar and V. Kumar, *J. Energy Storage*, 2023, **71**, 108132.

56 M. Xu, Y. Li, M. Ihsan-Ul-Haq, N. Mubarak, Z. Liu, J. Wu, Z. Luo and J. K. Kim, *Energy Storage Mater.*, 2022, **44**, 477–486.

57 J. Qian, C. Wu, Y. Cao, Z. Ma, Y. Huang, X. Ai and H. Yang, *Adv. Energy Mater.*, 2018, **8**, 1702619.

58 H. Yang, W. Tian, X. Chen, Z. Li, P. Liu, Q. Wang, X. Nie, Q. Wang and L. Jiao, *Batter. Supercaps*, , DOI:10.1002/batt.202400383.

The data supporting this article have been included as part of the ESI.